AIAA JOURNAL
Vol. 48, No. 10, October 2010

Computation of High-Speed Coaxial Jets with Fan Flow Deflection

Juntao Xiong,* Preben Nielsen,† Feng Liu,‡ and Dimitri Papamoschou§
University of California, Irvine, Irvine, California 92697

DOI: 10.2514/1.J050331

We present a computational study, validated by mean-flow experiments, of a dual-stream nozzle simulating the exit conditions of a supersonic turbofan engine with noise-suppressing fan flow deflectors. The study is conducted for eight nozzle configurations and two operating conditions: a cold condition at which mean velocity surveys were conducted and against which the computational code was validated and a hot condition that corresponds to the takeoff engine cycle and at which acoustic data were collected. The code predictions successfully replicate the mean velocity fields and the inflectional layers of the experimental flows. The code is then extended to the conditions of the actual engine cycle. The computations reveal a similar velocity profile for the hot and cold conditions when the axial distance is normalized by the potential core length. For both conditions, the vane deflectors reduce the turbulent kinetic energy k on the underside of the jet. An overall noise source strength is modeled as the axial integral of $k^{7/2}$. A significant correlation is found between the reduction in the noise source strength and the reduction in the peak level of the overall sound pressure level.

Nomenclature

A	=	area
a	=	speed of sound
c	=	vane chord length
D_f	=	nozzle fan diameter
E	=	total internal energy
F_c	=	inviscid convective flux
F_d	=	viscous diffusive flux
k	=	turbulent kinetic energy
$k_{\max}$	=	maximum k along a given radial direction.
k_{peak}	=	maximum k on a given azimuthal plane $\phi = \phi_0$
M	=	Mach number
NPR	=	nozzle pressure ratio
$\mathbf{P}_c$	=	preconditioning matrix based on conservative variables
$\mathbf{P}_o$	=	preconditioning matrix based on primitive variables
p	=	pressure
r	=	radial direction
s	=	entropy
U	=	nozzle exit or ambient velocity
$\mathbf{u}$	=	velocity vector (u, v, w)
$\mathbf{W}$	=	conservative variable vector
$\mathbf{W_0}$	=	primitive variable vector
x	=	axial direction (from plug tip)
y	=	vertical transverse direction
z	=	horizontal transverse direction
α	=	vane angle of attack
θ	=	polar angle from jet axis
μ_L	=	molecular viscosity
μ_T	=	turbulent viscosity
ρ	=	density
$\boldsymbol{\tau}$	=	stress tensor
ϕ	=	azimuth angle from downward vertical
Ω	=	vorticity
ω	=	specific dissipation rate or frequency

Subscripts

p	=	primary (core) exhaust
s	=	secondary (fan) exhaust
∞	=	freestream

Presented as Paper 2009-3254 at the 15th AIAA/CEAS Aeroacoustics Conference, Miami, FL, 11–13 May 2009; received 4 November 2009; revision received 12 March 2010; accepted for publication 27 March 2010.

*Postdoctoral Researcher, Department of Mechanical and Aerospace Engineering. Member AIAA.
†Graduate Researcher, Department of Mechanical and Aerospace Engineering. Student Member AIAA.
‡Professor, Department of Mechanical and Aerospace Engineering. Associate Fellow AIAA.
§Professor, Department of Mechanical and Aerospace Engineering. Fellow AIAA.

I. Introduction

THE coaxial jet with normal velocity profile has flow features that can be controlled to reduce sound in azimuthal directions of relevance to aircraft noise. To appreciate these features, let us outline the key difference between a single round jet and a coaxial jet. The single jet comprises an annular shear layer that surrounds the potential core and merges onto itself at the end of the potential core. Downstream of the potential core the velocity decays rapidly. Noise is generated by the entire shear layer and a small portion of the flow past the potential core. The near field of the coaxial jet consists of a primary (inner) shear layer between the primary and secondary streams, and a secondary (outer) shear layer between the secondary stream and the ambient fluid. For typical primary-to-secondary area ratios and velocity ratios used in turbofan engines, the inner and outer shear layers merge before the end of the primary potential core. Upstream of the merge point, in the so-called initial region, the potential core is surrounded by the secondary (outer) flow. Downstream of the merge point, the primary core is surrounded by the ambient fluid. The seminal coaxial jet experiments of Ko and Kwan [1] showed that for velocity ratios greater than 0.5, the secondary flow suppresses turbulence levels of the inner shear layer in the initial region of the jet. This feature is prominent in the coaxial jet noise model of Fisher et al. [2], wherein the primary shear layer in the initial region of the jet is treated as making negligible contribution to noise.

Noise generation by the turbulent jet is an extremely complex phenomenon and the subject of intense scrutiny and debate. Here we present two simplified views of noise generation that are relevant to the noise-suppression method of this paper. First, we can connect noise generation to the turbulent kinetic energy (TKE), k, in the sense that the square root of k describes a characteristic velocity associated with the Lighthill stress tensor [3]. In prevailing acoustic analogy models [3–5] the noise source is a strong function of the TKE, scaling as $k^{7/2}$. The second viewpoint is based on noise generation by instability waves, a concept whose foundation was laid by the experiments of Troutt and McLaughlin [6] and the stability analysis of Tam and Burton [7]. Sound radiation from large-scale turbulent

structures (modeled as instability waves) is a strong function of the convective Mach number M_c and the amplitude modulation of the instability. It should be noted that traditional acoustic analogy models are inherently applicable for noise emitted at large polar angles to the jet axis ($\theta \sim 90°$). For noise at small angles, near the direction of peak emission, the large-scale instability model may be more appropriate. Nevertheless, acoustic analogy models with appropriate directivity functions have shown reasonable predictions of noise at large and small angles [5]. We expect indeed a qualitative correlation between the convective Mach number and the turbulent kinetic energy: both depend on the mean velocity difference across the turbulent region of interest. High-gradient regions are expected to have high local values of k and M_c. Reynolds-averaged Navier–Stokes (RANS) computation, the tool used here, does not have the ability to resolve instability phase speeds, and therefore M_c, but can provide reasonable estimates of k. The hypothesis of this study is that the source that generates the peak noise is a strong function of k, and that a change of k in a particular azimuthal direction changes the sound emission in that direction. The implied causal relation between turbulence and sound in the direction of peak emission is supported by experiments wherein *point* measurements of turbulence fluctuations were found to correlate strongly with far-field pressure fluctuations in the direction of peak emission [8].

In the turbulent jet, both k and M_c have a finite lifespan. The TKE starts at a low level at the nozzle exit, peaks near the end of the potential core, then decays rapidly downstream. The convective Mach number exhibits a similar trend [9]. If we were to contemplate noise reduction by decreasing k or M_c, we only need to worry about the region from the nozzle exit up to a couple of diameters past the end of the potential core. In the initial region of the coaxial jet, the reduced velocity difference across the inner shear layer leads to a reduction of both k and M_c. Concentration of the secondary flow on the underside of the jet, using offset nozzles or fan flow deflectors, has been shown to extend this initial region, leading to substantial downward reduction of noise in both supersonic [10,11] and subsonic [12–15] jets. Experiments in large-scale NASA facilities, and RANS computation of the flowfields, have shown significant reduction of k on the underside of the jet with application of offset nozzles or fan flow deflectors [15]. Comparable results have been observed in joint experimental and large eddy simulation studies of beveled nozzles [16].

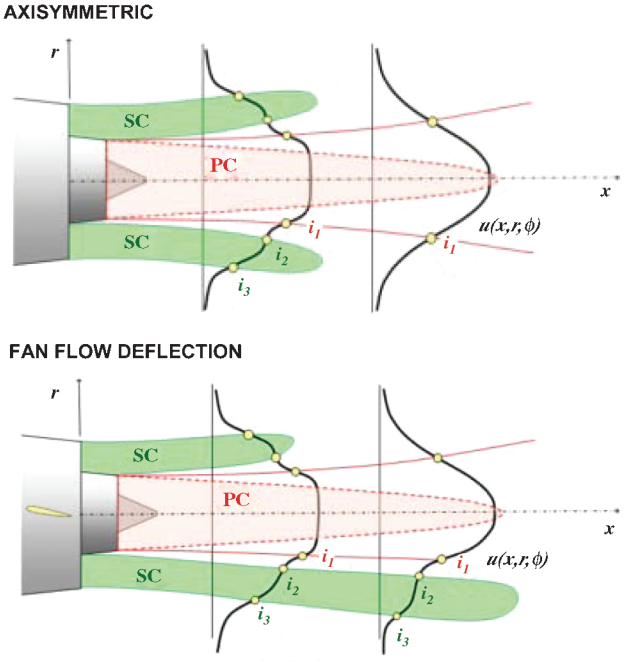

Fig. 1 Principal features of mean velocity field in a coaxial jet with regard to noise generation and their distortion by means of fan flow deflection.

In this study we investigate the ability of RANS computations to capture the salient elements of coaxial jets vis-à-vis noise generation and noise reduction. The validation basis is mean-flow experiments performed in cold jets. We will compare not only the velocity profiles but also inflectional layers that we believe play a strong role in noise suppression [9]. The definition and role of the inflectional is explained in the diagram of Fig. 1. The primary core (PC) is defined as the region where the velocity exceeds a high threshold, typically 80–90% of the core exit velocity, and represents the region of the most intense noise sources. The secondary core (SC) is defined by the outer inflection points i_2 and i_3 of the radial velocity profile, which naturally form a loop and thus define the initial region of the jet. Extension of the secondary core, in relation to the length of the primary core, reduces the convective Mach number and TKE of the inner shear layer.

The overall computational and validation approach is similar to those used by Dippold et al. [15] and DeBonis [17] in offset nozzle flows, although the emphasis here is on high-speed jets and the validation includes the aforementioned inflectional layers. In addition, there are some differences in the details of the computation that will be discussed later. Once the validation is confirmed, the code is then extended to hot jets representing the actual takeoff engine cycle. A discussion on the comparison between cold and hot velocity fields is presented. Finally, turbulence data for various fan flow deflection configurations, computed at the hot cycle point, conditions are presented and preliminary correlations are drawn between the reduction in turbulent kinetic energy and the reduction in overall sound pressure level measured in the acoustic experiments.

II. Experimental Setup

In this section we present the experimental nozzle configuration along with a brief overview of the diagnostic methods. The reader may consult past reports for a more thorough description of the measurement procedures [14]. The nozzle design in this study is based on the 3BB separate-flow nozzle developed at NASA John H. Glenn Research Center at Lewis Field [18], nominally for bypass ratio BPR = 5. The fan duct was reduced in diameter to produce BPR = 2.7 at the takeoff cycle point and the entire nozzle was scaled down by factor of 8 to fit within the flow rate capability of our test rig. The fan exit diameter was $D_f = 28.1$ mm, and the fan exit height was 1.8 mm. The nozzle construction and coordinates are shown in

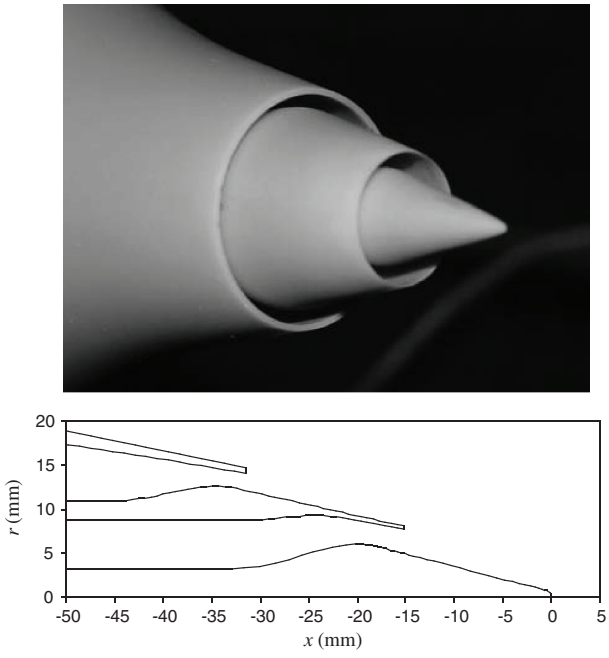

Fig. 2 Assembled nozzle and coordinates of the bypass ratio BPR = 2.7 nozzle.

Table 1 Exhaust conditions

	Hot (cycle point)	Cold
U_p, m/s	600	319
M_p	1.03	1.03
NPR_p	2.00	1.96
U_s, m/s	400	213
M_s	1.15	0.65
NPR_s	2.25	1.33
A_s/A_p	1.40	1.40
U_s/U_p	0.67	0.67

Fig. 2. The baseline nozzles were fabricated using a rapid-prototyping epoxy method.

The nozzle was tested at two set points. The first set point, labeled hot, corresponds to the takeoff engine cycle conditions as determined by earlier studies [11], with bypass ratio 2.7, fan pressure 2.2, and primary exhaust velocity $U_p = 600$ m/s. These conditions were replicated in the aeroacoustic tests using helium–air mixture jets, which have been shown to match very well the acoustics of hot-air jets [19]. The second set point, labeled cold, involved cold-air jets at the same primary Mach number and same secondary-to-primary velocity ratio as the hot set point. The conditions for the two set points are summarized in Table 1. For convenience, we will refer to these two set points as hot and cold, realizing that they involve not only temperature (density) differences but also Mach number differences. The Reynolds number of the jet, based on fan diameter, was 0.92×10^6 in the hot tests and 0.47×10^6 in the cold tests.

Fan flow deflection was achieved through the use of internal airfoil-shaped vanes that spanned the width of the annulus of the fan nozzle. Figure 3 illustrates the geometric parameters of the vanes. The vanes were micromachined from high-strength polycarbonate material using CAD/CAM facilities (Roland MDX-40 subtractive rapid-prototyping milling machine). The vane cross sections encompassed symmetric and asymmetric airfoils with NACA 0012, 4412, and 7514 shapes. The base and tip of each vane were shaped to conform to the geometry of the fan and core ducts at the exact location where the vane was attached. The vane chord length was $c = 3$ mm and the vane trailing edge was situated at $x_{\text{te}} = 2$ mm upstream of the nozzle exit. Nozzles were tested with both single-pair (2V) and two-pair (4V) vane configurations at various azimuth angles and angles of attack. Table 2 lists the geometric parameters of the deflectors and acoustic results to be discussed later.

Aeroacoustic tests were conducted in the University of California, Irvine's Jet Aeroacoustics Facility, a subscale facility (approximately one-fiftieth of full scale for the tests in question) that uses helium–air mixtures for replicating the exhaust velocity and density of hot jets [19]. In the present tests, the hot conditions of the BPR = 2.7 cycle were matched (Table 1). Jet noise was recorded by a far-field microphone array consisting of eight 3.2 mm condenser microphones (Bruel & Kjaer, model 4138) arranged on a circular arc centered at the vicinity of the nozzle exit. This study encompassed the azimuth angles $\phi = 0°$ (downward) and $\phi = 60°$ (sideline). Data from the microphone array were processed into lossless narrowband sound pressure level (SPL) spectra whose integration yielded the overall sound pressure levels (OASPLs). This report considers only the OASPL, plots of which will be shown later. The reduction in the peak level of OASPL is listed in Table 2. More extensive acoustic data for these types of flows can be found in [10].

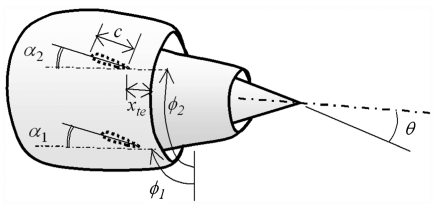

Fig. 3 Geometric parameters of vanes and definition of polar angle θ.

Table 2 Fan flow deflector configurations and reductions in peak OASPL

Configuration	Airfoil	α_1, deg	ϕ_1, deg	α_2, deg	ϕ_2, deg	$-\Delta$OASPL, dB (down/side)
Baseline	——	——	——	——	——	0.0/0.0
2Va	0012	7.5	90	——	——	1.5/1.6
2Vb	0012	7.5	150	——	——	0.4/0.8
2Vc	7514	4.0	120	——	——	2.7/2.5
4Va	7514	4.0	50	4.0	120	4.8/4.0
4Vb	0012	7.5	90	7.5	150	3.5/3.1
4Vc	4412	7.5	90	4.0	150	3.2/3.7
4Vd	7514	4.0	50	4.0	90	4.3/2.5

Each acoustic test was followed by a mean velocity survey in a duplicate dual-stream rig on which the identical nozzles and deflectors were installed. Because of large run times, pure air was used in both primary and secondary streams instead of the helium–air mixtures used in the acoustic tests. Therefore, the flow velocities were lower than those in the acoustic tests. However, the velocity ratio and primary Mach number were held the same as in the acoustic tests, as shown in Table 1. The mean axial velocity in the jet plume was surveyed using a Pitot rake system consisting of five probes, spaced apart by 10 mm, with hypodermic 0.5-mm-i.d. tips. Mounted on a three-dimensional motorized traverse, the rake scanned the entire jet plume up to 12 fan diameters from the nozzle exit. The velocity was computed from the Pitot measurements under the assumptions of constant static pressure (equal to ambient pressure) and constant total temperature (equal to room temperature). Smoothing of the velocity profiles and computation of the velocity derivatives was performed using a Savitzky–Golay filter [20]. The inflectional layers were identified by locating the zeros of the second radial derivative of the mean velocity.

In computing radial velocity derivatives (based on which the inflectional layers are identified), it is important to define a proper center for the jet. This is also relevant to the evaluation of TKE in particular azimuthal directions, to be performed in Sec. VII. The fan flow deflectors impart a slight downward tilt to the jet column but also deform appreciably the velocity profile. Past works on asymmetric incompressible jets [21,22] used the centroid of the velocity profile to define the center of the jet. Here we extend this method to compressible jets by using the centroid of the mass flux ρu. We note that center definitions based on the centroids of the velocity u or the momentum flux ρu^2 yielded very similar results. Figure 4 illustrates the radial-azimuthal coordinate system based on the centroid of the mass flux.

III. Computational Method

The computational fluid dynamics code used here is known as ParCAE and solves the unsteady three-dimensional RANS equations on structured multiblock grids using a cell-centered finite volume method with artificial dissipation as proposed by Jameson et al. [23]. Information exchange for flow computation on multiblock grids

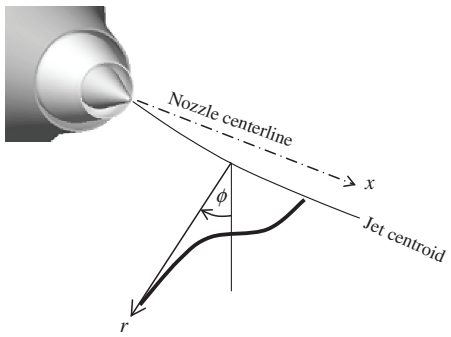

Fig. 4 Definition of radial r and azimuthal ϕ coordinate system used in computation of radial derivatives and identification of TKE maximum.

using multiple CPUs is implemented through the message-passing-interface protocol. The RANS equations are solved using the eddy-viscosity-type turbulence models. The code contains the Baldwin–Lomax algebraic model [24], the one-equation Spalart–Allmaras [25] turbulence model, the two-equation k-ω model of Wilcox [26] and the shear stress transport (SST) turbulence model by Menter [27]. In this study, only the steady-state solution is obtained because we are interested in the time-averaged features of the flow. The SST turbulence model combines the advantages of the k-ω and k-ε turbulence models to give superior performance in simulating the wall boundary layer and freestream flow, thus the SST model is chosen for all the cases in this work. The main elements of the code are summarized below.

The differential governing equations for unsteady compressible flow can be expressed as follows:

$$\frac{\partial \mathbf{W}}{\partial t} + \nabla \bullet (\mathbf{F}_c - \mathbf{F}_d) = 0 \tag{1}$$

The vector $\mathbf{W}$ contains the conservative variables $(\rho, \rho u, \rho v, \rho w, \rho E)^T$. The fluxes consist of the inviscid convective fluxes $\mathbf{F}_c$ and the diffusive fluxes $\mathbf{F}_d$, defined as

$$\mathbf{F}_c = \begin{pmatrix} \rho u & \rho v & \rho w \\ \rho uu + p & \rho uv & \rho uw \\ \rho vu & \rho vv + p & \rho vw \\ \rho wu & \rho wv & \rho ww + p \\ \rho Eu + pu & \rho Ev + pv & \rho Ew + pw \end{pmatrix} \tag{2}$$

$$\mathbf{F}_d = \begin{pmatrix} 0 & 0 & 0 \\ \tau_{xx} & \tau_{xy} & \tau_{xz} \\ \tau_{yx} & \tau_{yy} & \tau_{yz} \\ \tau_{zx} & \tau_{zy} & \tau_{zz} \\ \Theta_x & \Theta_y & \Theta_z \end{pmatrix} \tag{3}$$

with

$$\Theta = \mathbf{u} : \boldsymbol{\tau} - \left(\frac{\mu_L}{Pr_L} + \frac{\mu_T}{Pr_T} \right) \nabla T$$

The stress tensor $\boldsymbol{\tau}$ depends on the viscosity $\mu = \mu_L + \mu_T$, where the subscripts L and T represent laminar and turbulent contributions, respectively. Pr_L and Pr_T are the laminar and turbulent Prandtl numbers, respectively.

The closure model used to evaluate the turbulent viscosity μ_T is the k-ω SST turbulence model, given by the equations

$$\begin{aligned} \frac{\partial \rho k}{\partial t} + \nabla \bullet (\rho k \mathbf{u} - \mu_k^* \nabla k) &= \rho S_k \\ \frac{\partial \rho \omega}{\partial t} + \nabla \bullet (\rho \omega \mathbf{u} - \mu_\omega^* \nabla \omega) &= \rho S_\omega \end{aligned} \tag{4}$$

where $\mu_k^* = \mu_L + \sigma_k \mu_T$, $\mu_\omega^* = \mu_L + \sigma_\omega \mu_T$, and $\mu_T = \rho a_1 k / \max(a_1 \omega, \Omega f_2)$. The source terms S_k and S_ω are

$$S_k = \frac{1}{\rho} \boldsymbol{\tau} : \nabla \mathbf{u} - \beta^* \omega k$$

$$S_\omega = \frac{\gamma}{\mu_T} \boldsymbol{\tau} : \nabla \mathbf{u} - \beta \omega^2 + 2(1 - f_1) \frac{1}{\omega} \nabla k \bullet \nabla \omega$$

In the above equations, f_1 and f_2 are blending functions. The parameters a_1, σ^*, σ_k, β, β^*, and γ are closure coefficients.

The flow and the turbulence equations were discretized in space by a structured hexahedral grid using a cell-centered finite volume method. Since within the code each block is considered as a single entity, only flow and turbulence quantities at the block boundaries needed to be exchanged. The governing equations were solved explicitly in a coupled manner through a five-stage Runge–Kutta scheme toward steady state with local time-stepping, residual smoothing, and multigrid for convergence acceleration. A distinction from past RANS computational studies of offset nozzle flows [15,17] is the use of the Jameson–Schmidt–Turkel dissipation scheme and a low-speed preconditioner [28], explained below, to handle the low ambient Mach number of the nozzle and jet plume flows. Further details of the numerical method can be found in [29].

The ParCAE code used in this investigation is designed for compressible flows. It is known that the numerical solution of a compressible flow solver may have difficulty converging to the physical incompressible flow as the freestream Mach number becomes very small because of the large disparity between flow velocity and acoustic wave speed. To fix this issue, the preconditioning technique proposed by Turkel [28] is applied wherein the unsteady term of Eq. (1) is multiplied by a preconditioning matrix $\mathbf{P}_c$:

$$\mathbf{P}_c \frac{\partial \mathbf{W}}{\partial t} + \nabla \bullet (\mathbf{F}_c - \mathbf{F}_d) = 0 \tag{5}$$

Preconditioning changes the eigenvalues of the system of compressible flow equations in order to remove the aforementioned disparity. It reaches the same solution to the original equations without the preconditioning once convergence is achieved. Determination of

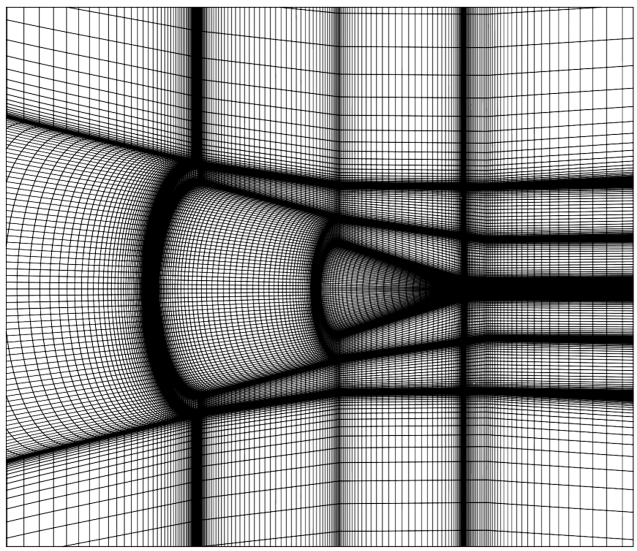

a)

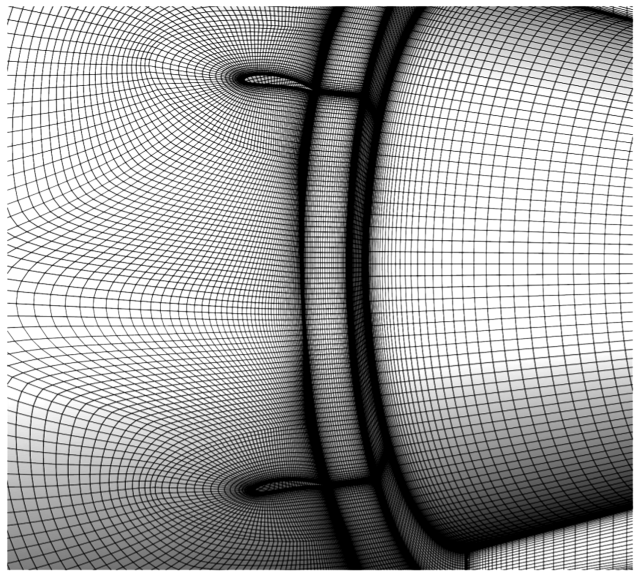

b)

Fig. 5 Computational grid: a) baseline nozzle and b) detail of the grid around the vanes.

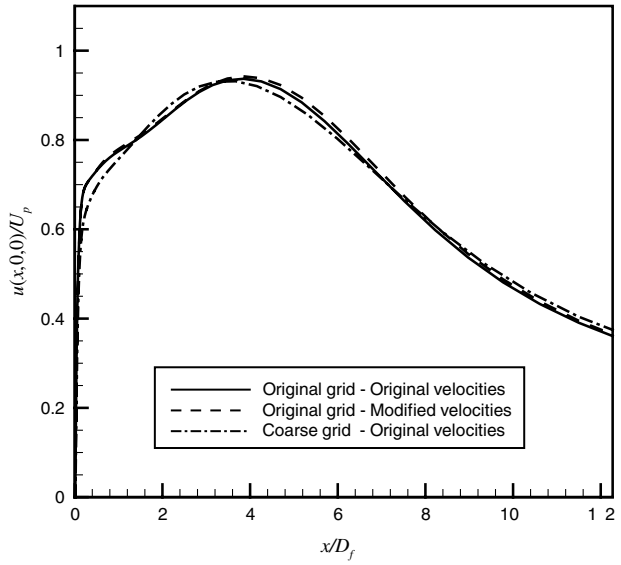

Fig. 6 Comparison of centerline velocity between different flow conditions and grids.

$\mathbf{P}_c$ involves the definition of an initial preconditioning matrix $\mathbf{P}_0$ for the primitive variable vector $\mathbf{W}_0 = (p, u, v, w, s)^T$:

$$\mathbf{P}_0 = \begin{bmatrix} \frac{a^2}{M_r^2} & 0 & 0 & 0 & 0 \\ 0 & 1 & 0 & 0 & 0 \\ 0 & 0 & 1 & 0 & 0 \\ 0 & 0 & 0 & 1 & 0 \\ 0 & 0 & 0 & 0 & 1 \end{bmatrix} \tag{6}$$

with

$$M_r^2 = \min\left\{\max\left[K_1 c^2 M^2\left(1 + \frac{1 - M_0^2}{M_0^4} M^2\right), K_2^2 U_\infty^2\right], a^2\right\}$$

where a is the local speed of sound, M_0 is a properly chosen reference Mach number to maintain stability of the computation, M is the local Mach number, and K_1 and K_2 are coefficients. The conservative preconditioning matrix is computed from the transformation:

$$\mathbf{P}_c = \frac{\partial \mathbf{W}}{\partial \mathbf{W}_0} \qquad \mathbf{P}_0 \frac{\partial \mathbf{W}_0}{\partial \mathbf{W}} \tag{7}$$

Even with the preconditioner, however, a numerical singularity arises at $M_\infty = 0$, necessitating a small forward velocity in the computations.

Multiblock grids were generated using ICEM-CFD for each vane configuration. As all the configurations were symmetric around the xy plane, only one-half of the nozzle was modeled to save computational expense. To simulate the jet flow, the grid extended about $3.8D_f$ radially outward from the nozzle centerline and over $20D_f$ downstream of the nozzle. The C-grid was used around each vane in the region near the exit plane to capture the features of boundary layer and wake flows accurately. The outer region grids for both cases were identical to simplify grid-generation work. The patch-connection interpolation technique [30,31] was then used to

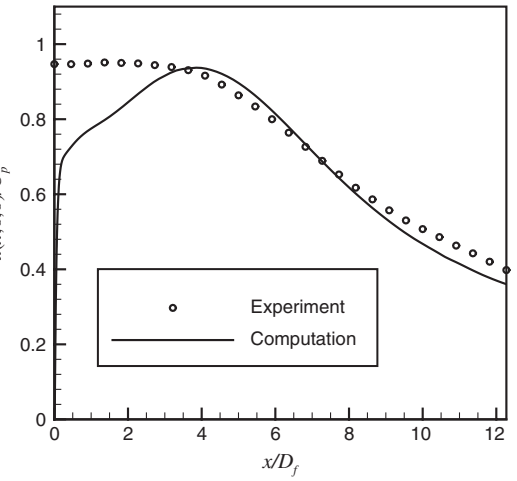

Fig. 8 Comparison of computational and experimental centerline velocity for the baseline nozzle.

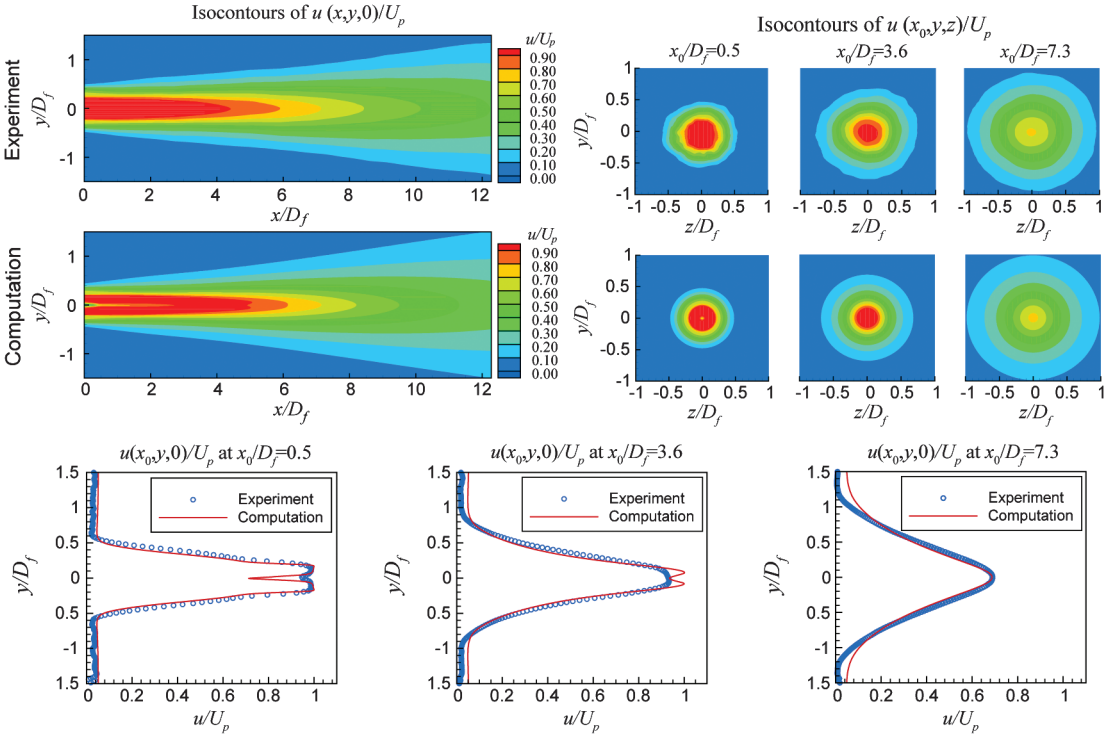

Fig. 7 Comparison of computational and experimental velocity field for the baseline nozzle.

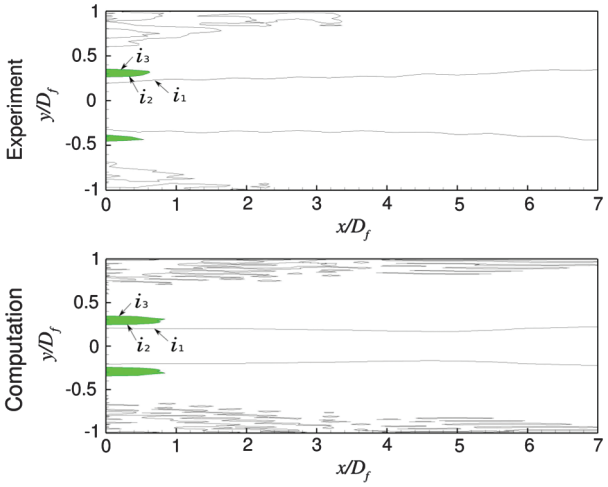

Fig. 9 Comparison of computational and experimental inflectional layers for the baseline nozzle.

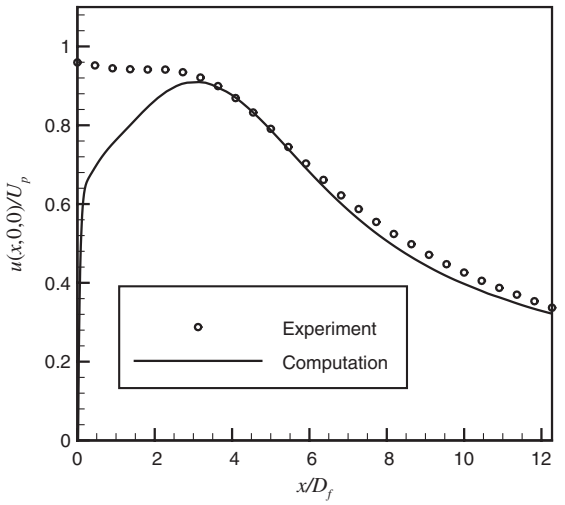

Fig. 11 Comparison of computational and experimental centerline velocity for the 4Va configuration.

transfer flow variable information between nonmatched connection surfaces. Figure 5 shows the whole nozzle grid and the grid around the vane. The grids were clustered all along the wall boundaries. The base nozzle grid had 3.7 million grid points. The two-vane and four-vane configurations had 4.9 million and 5.8 million grid points, respectively. For all the grids, the minimum y^+ of the first grid point from the wall was less than 1. The average y^+ values were about 3. Wall functions were not required. The grids were divided into multiblocks to implement parallelization on multiprocessors computers to reduce convergence time. Convergence was determined once the average residuals of both the continuity and momentum equations decreased at least 3 orders of magnitude and the changes of the residuals between successive iterations reduced to the order of 0.01%.

The computations were performed at both the hot and cold set points of Table 1. The cold computations were used for validation against the experimental mean-flow data. The hot computations yielded turbulence data that could be correlated with the experimental acoustic results. Even though the experiments were performed at static ambient conditions, for numerical stability the computations were run with a freestream velocity of 17 m/s ($M_\infty = 0.05$). For the fan and core duct flows, uniform total pressure was specified at the inlet surface corresponding to the perfectly expanded exit Mach number. For the ambient region surrounding the nozzle flow, a characteristic boundary condition was defined, and the downstream static pressure was set to the ambient pressure. Adiabatic no-slip boundary condition was specified on all nozzle and vane solid walls. The jet Reynolds numbers matched the experimental values given in Sec. II.

We conducted two sensitivity studies, the first to test grid independence and the second to assess the effect of the small forward velocity on the computational results. Grid independence was evaluated by reducing the number of grid points by 50% (21% in each spatial direction). The effect of the 17 m/s ambient velocity was evaluated by augmenting the core and fan velocities (cold conditions) by 17 m/s, thus maintaining the same velocity differences between

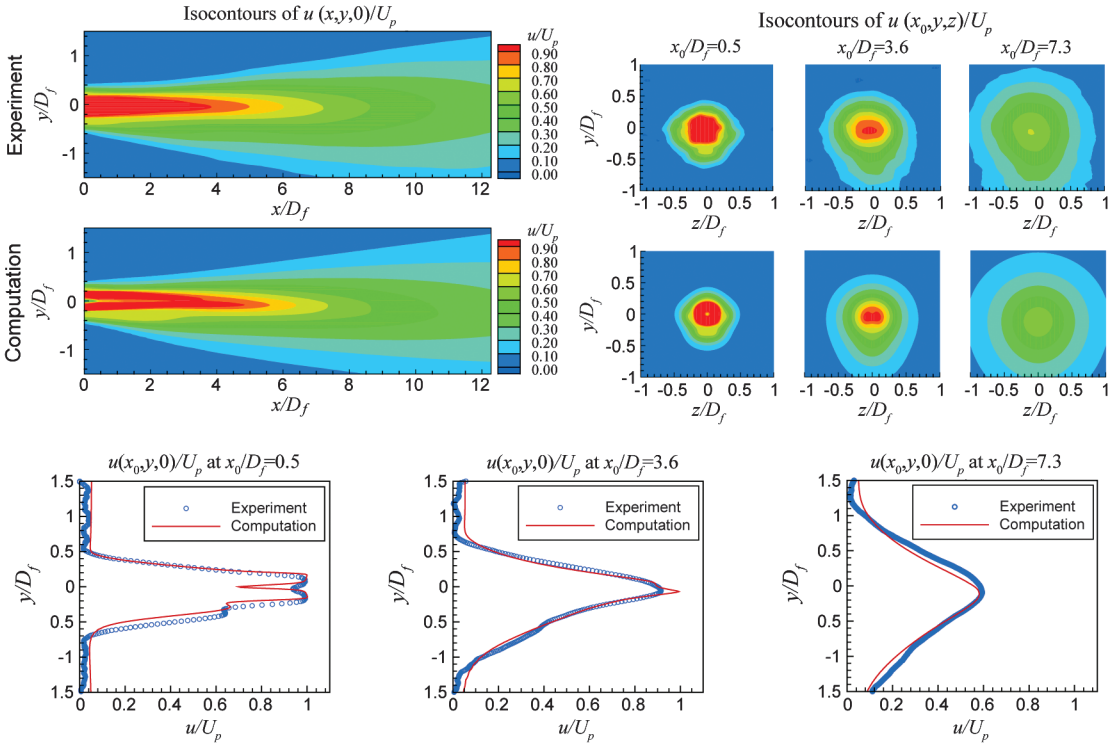

Fig. 10 Comparison of computational and experimental velocity field for the 4Va configuration.

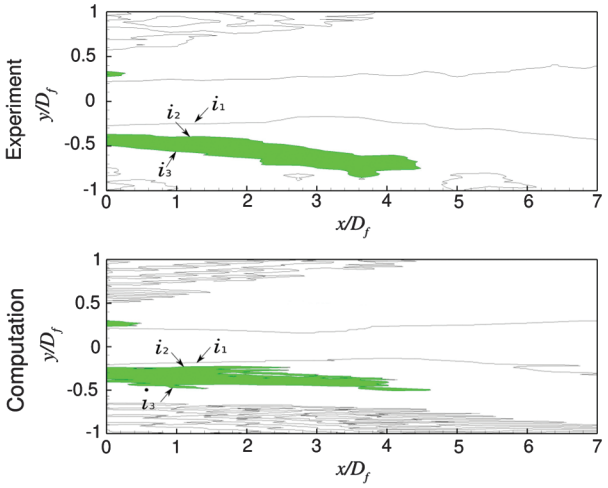

Fig. 12 Comparison of computational and experimental inflectional layers for the 4Va configuration.

jet flows and ambient as in the experiments. The impacts of both sensitivity studies on the centerline velocity distribution of the baseline nozzle are shown in Fig. 6. The changes are negligible, indicating adequate grid resolution and minimal impact of the forward velocity on the results. Examination of velocity and turbulent kinetic energy profiles showed the same kind of insensitivity to grid refinement and forward velocity.

IV. Validation of the Computational Code

The basis for the validation of the computational code is comparison with experimental data of mean velocity and inflectional layers. In this report we compare velocity contour plots along the symmetry (xy) plane, transverse velocity contour plots at various axial locations downstream of the jet exit, and velocity line profiles along the vertical symmetry plane at various axial locations. Also presented are comparison plots of inflection layers, highlighting the generalized secondary core on the symmetry plane.

The results for the baseline nozzle are shown in Figs. 7–9. The velocity plots (Fig. 7) indicate good agreement between the experimental measurements and the computational simulation in the principal features of the flowfield. The potential core lengths are very similar at approximately $x/D_f = 5$. The growth rate of the computational and experimental jets are also very similar, as evidenced in the transverse contour plots and the overlapping of the velocity line plots. One distinction is that the computation resolves a stronger wake than does the experiment. The computation indicates that the wake region is very thin; it is thus and probable that the finite spatial resolution of the experimental measurement, defined by the probe diameter, smoothed out the details of the wake region. A comparison of the centerline velocity of the computational and experimental jets is shown in Fig. 7. The influence of the plug wake is seen to extend to $x/D_f = 3$ after which the centerline velocities are quite similar. We believe that the discrepancy in the thin wake region bears little impact on the principal trends and conclusions of this study.

Figure 9 presents the loci of the radial inflection points of the baseline velocity field for the experiment and the computation. Referring to the definitions of Fig. 1, the inner-most line is the locus of i_1. Around it forms the i_2-i_3 loop, which is highlighted for convenience. As explained in the Introduction, the i_2-i_3 loop defines the generalized secondary core. Further out radially are trivial inflectional points due to noise in the experimental and computational data toward the edge of the jet. Comparing the experimental and computational secondary cores we note a strong similarity in their lengths and shapes. There is a small difference in the radial location of the primary inflectional point i_1, mainly in the vicinity of $x/D_f = 6$, where the computation predicts a thinner primary inflection layer than the experiments. This is also evidenced in the velocity line plots in Fig. 7, where the computational line plots are slightly thinner and more peaky than the experimental plots.

The same types of comparisons are shown for the 4Va nozzle in Figs. 10–12. As with the baseline case, the velocity contour and line plots (Fig. 10) are all in good agreement. The potential core lengths are slightly different, as evidenced in the velocity contour plot along the vertical symmetry plane, with the experimental data showing a slightly shorter potential core than the computation. However, the general deflection of the jet is very similar. Particularly notable is the

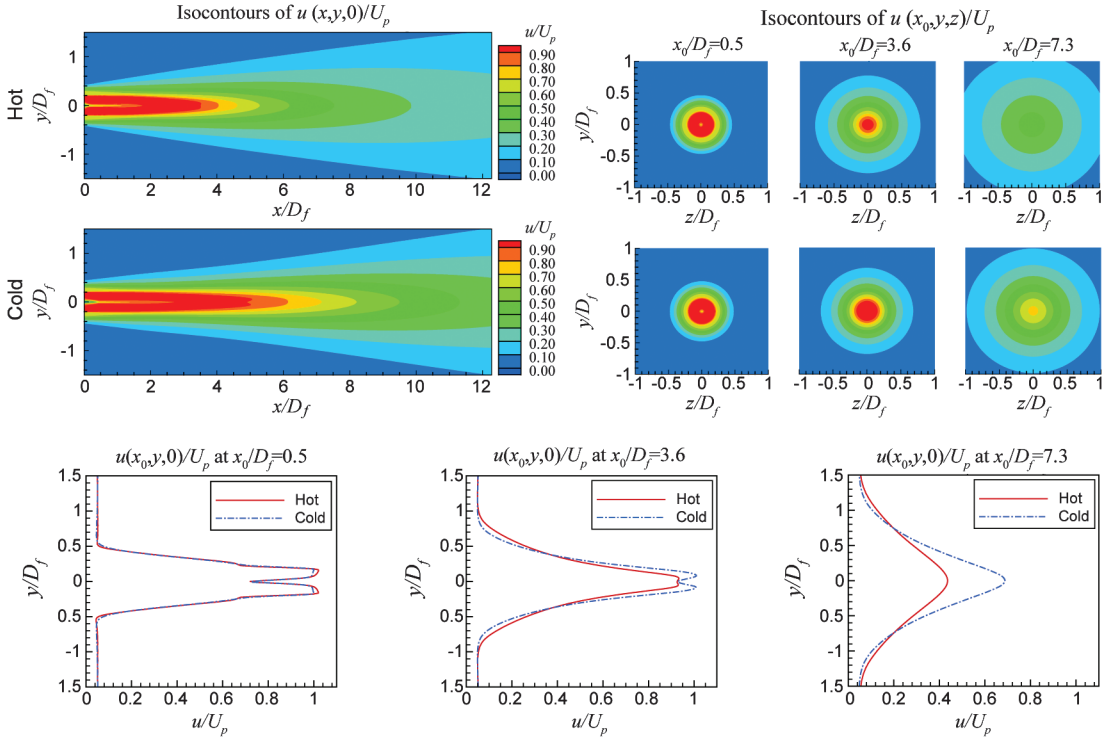

Fig. 13 Comparison of velocity profiles for hot and cold operating conditions for the baseline nozzle.

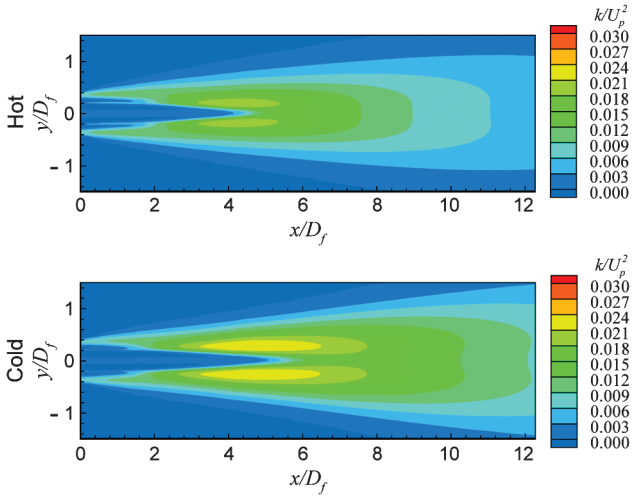

Fig. 14 Comparison of turbulent kinetic energy on the vertical symmetry plane for hot and cold operating conditions for the baseline nozzle.

similarity in shape of the computational and experimental transverse velocity contour plots. The centerline velocity plots of Fig. 10 show a good match of the axial velocity decay. Again the plug wake of the computational field is seen to influence the near field centerline velocity. In Fig. 12 we note that the computation reproduces with high fidelity the experimental inflectional layers. The lengths of the generalized secondary cores on the top and bottom of the jet are equal and the shapes of the primary inflection layers are very comparable.

Detailed comparisons between experimental and computational velocity fields for all the remaining cases of Table 2 showed similar agreements and are thus omitted for brevity. The success of the computational code in matching the cold experimental mean-flow data provided confidence in its ability to resolve the velocity field of the hot set point and provide important quantities, such as turbulent kinetic energy, that are critical to noise prediction and very difficult to measure experimentally.

V. Temperature Effects

The mean velocity experiments from which the computational code was validated were performed using cold conditions that matched the velocity ratio and primary Mach number of the hot conditions (Table 1). Given the success of the code in predicting the cold mean velocity field, we use it to study the differences between the velocity fields, including turbulent statistics, of the hot and cold jets. We note that the difference between the two conditions of Table 1 is not solely an increase in temperature. The Mach numbers of the internal and external flows are also different. With regard to the internal flow, the vanes at the hot set point operate in a higher Mach number environment than the vanes at the cold set point. This could induce subtle changes in the deformation of the mean flow. As far as the overall development of the plume is concerned, we expect that the elevated temperature (decreased density) produces major changes so we focus on its effect on the velocity and turbulent kinetic energy (TKE) fields. For brevity, in this section we cover two cases, the baseline nozzle and fan flow deflector configuration 4Va. The mean velocity results are presented in the same manner as in the previous section, and the TKE results are shown as contour plots of the symmetry plane and, in the cases of deflected flow, contour plots on several transverse planes. The TKE is presented in the normalized form $k^* = k/U_p^2$. The notation peak TKE (k^*_{peak}) signifies the maximum value of normalized TKE on a given azimuthal plane $\phi = \phi_0$ originating from the jet centroid.

The effects of temperature on the mean velocity field of the baseline case are depicted in Fig. 13. The velocity contour plots and line plots show a significantly larger growth rate for the hot jet, which results in shorter primary potential core for the hot jet compared to the cold. The plots of Fig. 14 show a compaction of the TKE contours with increasing temperature, again reflecting the faster spreading rate of the hot jet. The peak value of TKE declines slightly from $k^*_{\text{peak}} = 0.0239$ for the cold jet to $k^*_{\text{peak}} = 0.0212$ for the hot jet. It is important to note that the location of the peak TKE, compared with the location of the end of the potential core, is consistent between the hot and cold jets.

Comparison plots for the 4Va configuration are shown in Figs. 15–17. The velocity contours and profiles of Fig. 15 show similar trends to the baseline case with the hot jet having a significantly shorter

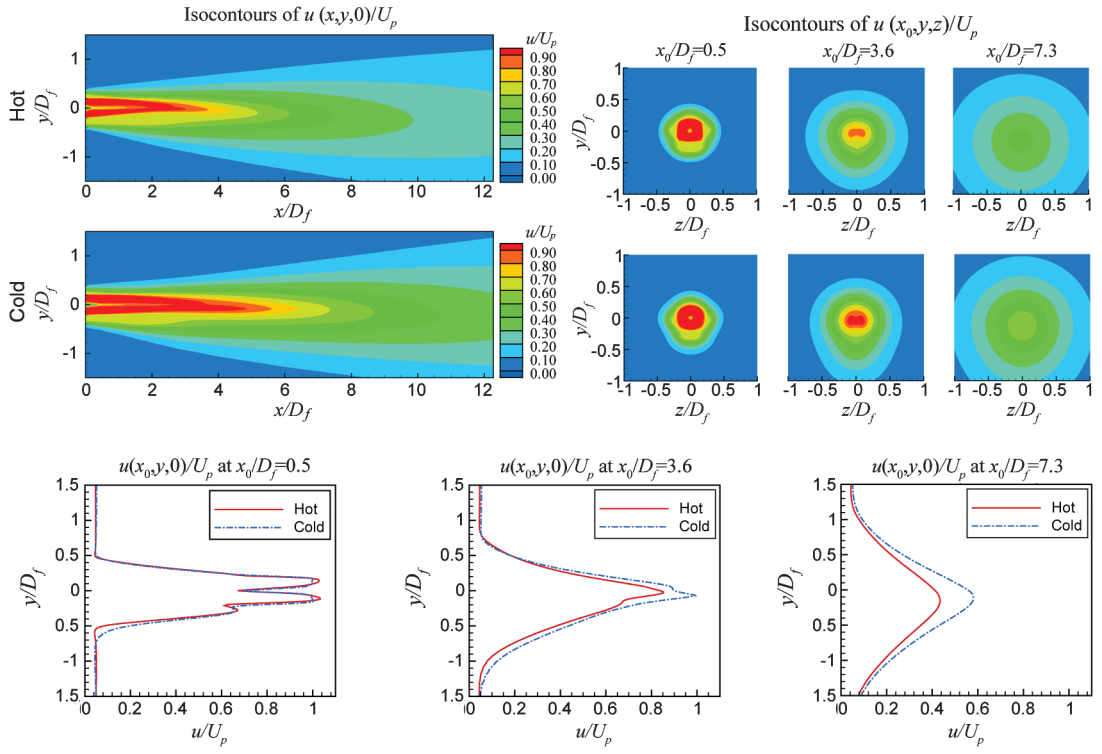

Fig. 15 Comparison of velocity profiles for hot and cold operating conditions for the 4Va configuration.

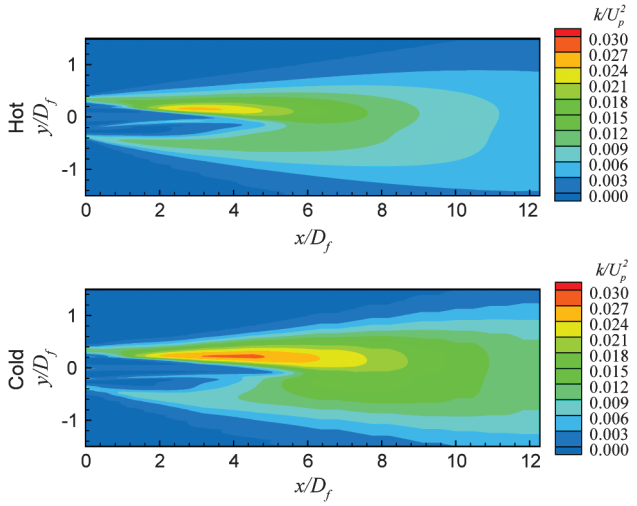

Fig. 16 Comparison of turbulent kinetic energy along the vertical symmetry plane for hot and cold operating conditions for the 4Va configuration.

potential core than the cold jet. The cold case has a slightly higher downward distortion, evidenced in the transverse velocity contour plots. The TKE contour plots of Figs. 16 and 17 highlight the effect of the flow deflection on the TKE distribution in the jet plume. The general trend is a reduction in TKE on the underside of the jet and increase on the top of the jet. As with the baseline case, the peak values of TKE are slightly smaller in the hot jet than in the cold jet. Considering the bottom of the jet ($\phi = 0$ deg), application of the deflectors 4Va reduces k^*_{peak} from 0.0239 to 0.0153 for the cold jet, and from 0.0212 to 0.0112 for the hot jet. In other words, the deflectors are more effective in reducing the peak TKE of the hot jet (47% reduction) than of the cold jet (36% reduction). At the top of the jet ($\phi = 180$ deg), the deflectors increase k^*_{peak} from 0.0239 to 0.0274 (13% increase) for the cold jet, and from 0.0212 to 0.0259 (22% increase) for the hot jet. Comparing the cross-sectional plots of Fig. 17, we note that the azimuthal extent of excess TKE at the top of the jet is more confined in the hot case.

As with the baseline case, the position of the peak turbulent kinetic energy with respect to the end of the potential core is the same in the hot and cold jets. In the previous figures, the velocity profiles for the cold and hot conditions were compared at the same axial distance (normalized by fan diameter). Given that a major effect of heating is reduction of the primary potential core length L_p, it is instructive to also compare profiles at the same x/L_p, with L_p defined as the axial distance from the nozzle plug where the maximum velocity equals 0.9 U_p. Such comparisons are shown in Figs. 18 and 19 for the baseline nozzle and the 4Va configuration, respectively. For the baseline nozzle the velocity profiles nearly collapse for the hot and cold cases when the axial location is nondimensionalized by the respective primary core length of each jet plume. A reasonable collapse also occurs for the 4Va fan flow deflection configuration. After accounting for the potential core length, Bridges [32] also observed the collapse of velocity profiles for single-stream jets with different temperatures. In a subsequent study Bridges and Wernet [33] additionally found that the spectral characteristics and space–time correlations of turbulence in the jet were temperature-invariant after taking into account the potential core length.

VI. Turbulent Kinetic Energy

In this section we examine key differences between the TKE distributions in the baseline and deflected jets. We consider only the hot cases. We already outlined principal trends in the previous section: the deflectors decrease the peak TKE on the underside of the jet and increase it on the top of the jet. Table 3 offers a more complete assessment of peak TKE for all the cases of this paper. It is seen that increases of peak TKE on the top of the jet are generally less than the corresponding decreases on the bottom of the jet. Also, appreciable TKE reductions persist on the $\phi = 60$ deg plane, which is critical for sideline noise reduction. We discuss here case 4Vc whose TKE field is plotted in Fig. 20. We compare it with the baseline TKE field of Fig. 14 (hot case).

For the baseline jet, the peak TKE occurs at $x/D_f = 4$, which is slightly upstream of the end of the primary potential core $x/D_f = 4.5$ (in the TKE contour plots, the primary potential core can be identified by the near-zero values of TKE around the jet axis). In the near field of the jet at $r/D_f \approx 0.2$, thin layers with small levels of TKE are apparent. They represent turbulence production by the inner shear layer between the primary and secondary streams. The turbulence level of the inner shear layer is much lower than that of the outer shear layer, consistent with the coaxial jet model of Fisher et al. [2] and the turbulence measurements of Ko and Kwan [1] at similar velocity ratios. For configuration 4Vc (Fig. 21), the TKE distribution on the bottom is very flat and it is difficult to pinpoint visually, from the figure, exactly where it peaks in the axial direction. The thin layer of TKE production by the inner shear layer is visible and elongated for the bottom part of the jet, reflecting the elongation of the downward secondary core, but is absent on the top of the jet, indicating the rapid depletion of the upward secondary core. On the top of the 4Vc jet, the TKE peaks upstream of the end of the potential core at around $x/D_f = 3.0$. The increase of TKE on the top of the jet, and the

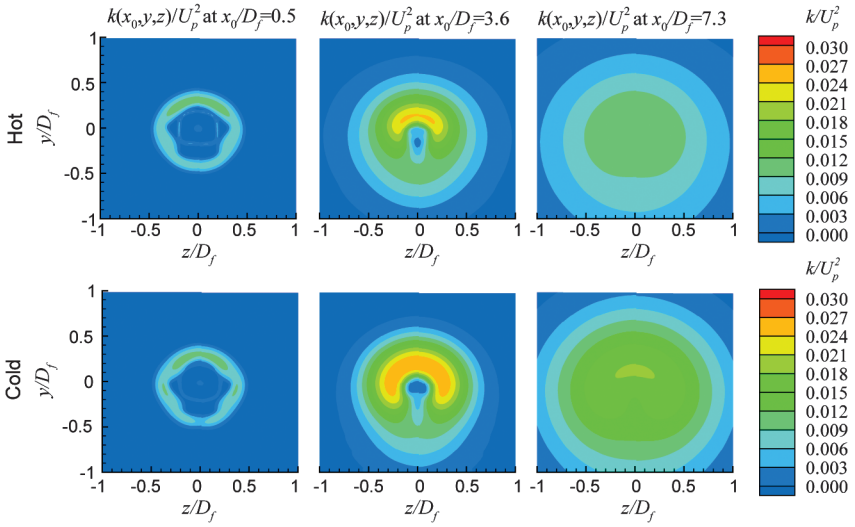

Fig. 17 Comparison of turbulent kinetic energy on the transverse plane at various axial distances for hot and cold operating conditions for the 4Va configuration.

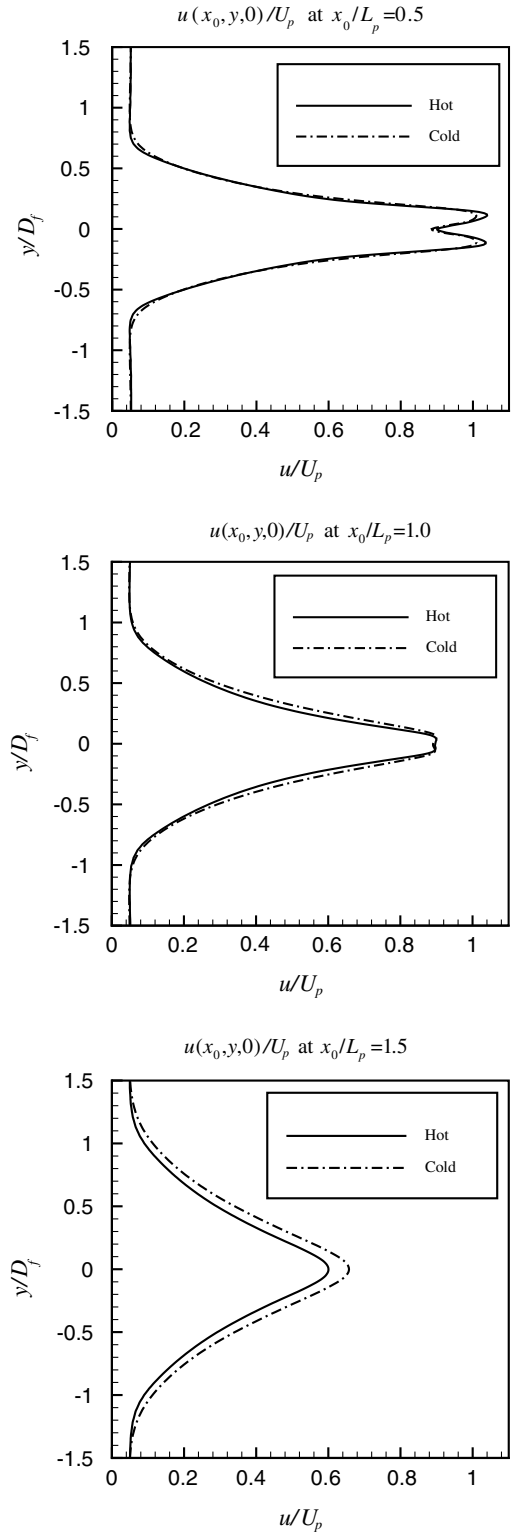

Fig. 18 Comparison of baseline velocity profiles at equal axial distances normalized by potential core lengths.

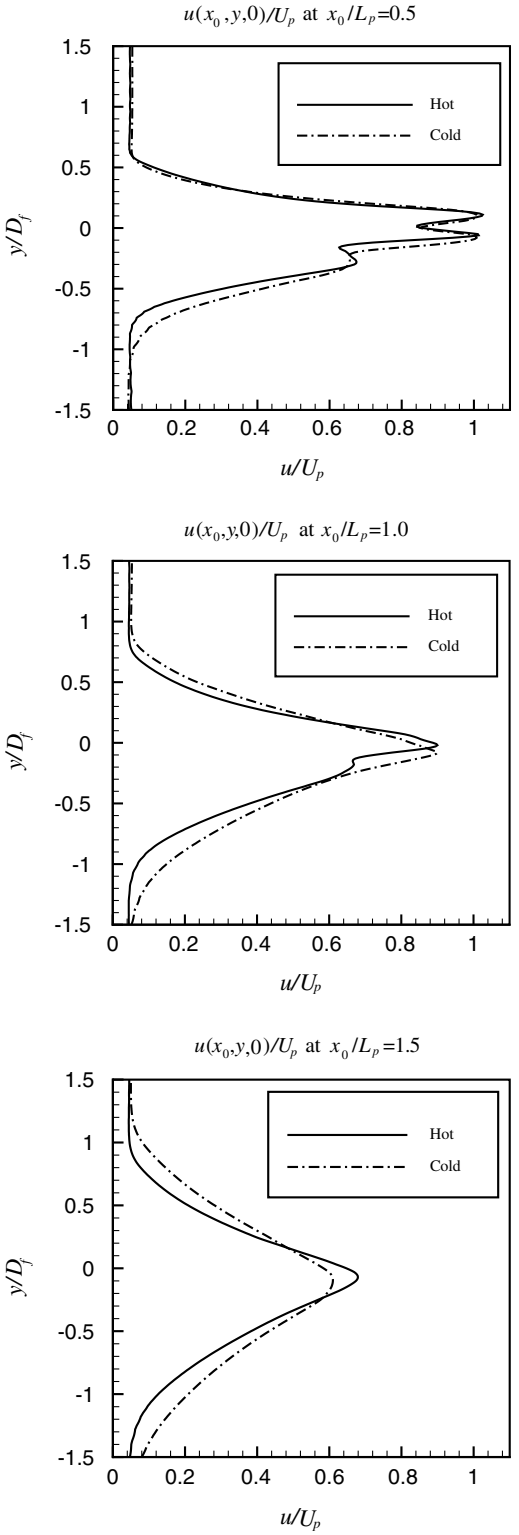

Fig. 19 Comparison of 4Va velocity profiles at equal axial distances normalized by the potential core lengths.

movement of its peak value closer to the nozzle, result from the shorter secondary core on the top of the jet, as exemplified in Fig. 12. In other words, on the top of the jet, the primary stream comes into contact with the ambient fluid a very short distance from the nozzle exit, resulting in strong velocity gradients and rapid TKE production. The transverse contour plots of Fig. 20 indicate that this excess TKE occurs in the azimuthal segment $|\phi| > 140$ deg. The TKE distributions without and with the fan flow deflectors are similar to those measured and computed in subsonic jets with large bypass ratios by Dippold et al. [15]. However, because the exhaust conditions are very different, direct comparisons with the results of [15] is not possible.

Further insight into the TKE behavior is gained by plotting the maximum value of TKE, $k^*_{\max}$, in given azimuthal direction ϕ as a function of x and ϕ. The maximum was determined by a computational search along a given azimuthal radial line at a fixed axial station. Figure 21a displays contour maps of $k^*_{\max}(x, \phi)$ for case 4Vc. The small levels of TKE at the bottom of the jet ($\phi \to 0°$) and large values at the top of the jet ($\phi \to 180°$) are evident. At the bottom of the jet, $k^*_{\max}$ peaks near $x/D_f = 6.0$, which is downstream of the

Table 3 Peak turbulent kinetic energy

Configuration	$\phi = 0°$ (down) k/U_p^2	Percent change	$\phi = 60°$ (side) k/U_p^2	Percent change	$\phi = 180°$ (up) k/U_p^2	Percent change
Baseline	0.0212	0.0%	0.0212	0.0%	0.0212	0.0%
2Va	0.0165	−22.2%	0.0175	−17.5%	0.0235	+10.8%
2Vb	0.0209	−1.1%	0.0202	−4.7%	0.0249	+17.5%
2Vc	0.0180	−15.1%	0.0165	−22.2%	0.0267	+25.9%
4Va	0.0112	−47.2%	0.0144	−32.1%	0.0259	+22.2%
4Vb	0.0149	−29.7%	0.0153	−27.8%	0.0265	+25.0%
4Vc	0.0125	−41.0%	0.0129	−39.2%	0.0268	+26.4%
4Vd	0.0103	−51.4%	0.0172	−18.9%	0.0230	+8.5%

end of the potential core. With increasing azimuth angle, the location of peak $k^*_{\max}$ shifts toward the nozzle exit, consistent with the observations stated previously. Figure 21b presents a differential map of $k^*_{\max}$ whereby the values of the baseline have been subtracted from the values of case 4Vc. This map highlights the changes in the TKE field due to the fan flow deflection. The reduction in $k^*_{\max}$ extends from $\phi = 0°$ to $\phi = 70°$ and is concentrated around $x/D_f = 4$. The increase of $k^*_{\max}$ extends from $\phi = 140°$ to $\phi = 180°$ and is concentrated around $x/D_f = 2$.

VII. Approximate Model for the Reduction in OASPL

A central goal of our investigation was to assess whether we can build an approximate engineering model that predicts the change in peak OASPL due to a redistribution of TKE from a *known baseline condition*. We chose the peak OASPL because of the inherently directional nature of the jet noise source that radiates in the direction of peak emission. This is consistent with the directional (in the azimuthal sense) nature of the noise-suppression method studied here. There is evidence that noise at large polar angles is affected by noise sources over the entire azimuthal extent of the jet [5], so we do not expect directional control of noise at large polar angles.

To gain insight in key trends in the TKE and OASPL, we plot in Fig. 22 the axial TKE distributions and OASPL directivities for cases 2Va and 4Va. The TKE is plotted for azimuthal angles $\phi = 0$, 60, and 180° (downward, sideline, and upward), and the OASPL is plotted for $\phi = 0$ and 60°. First we note that the OASPL reductions occur primarily in the direction of peak emission. There is a correspondence between the reduction of OASPL and the magnitude and extent of the TKE reduction. For case 2Va, the TKE reduction is noticeable but moderate, and its axial extent is about $2.5D_f$. The reduction is practically equal for $\phi = 0°$ and 60°. On the top side of the jet, $\phi = 180°$, there is a small increase in the TKE level. The corresponding OASPL plots show a moderate reduction of 1.5 dB, equal for downward and sideline, in the direction of peak emission near $\theta = 45°$. For $60° < \theta < 80°$ the OASPL curves of 2Va virtually coincide with the baseline, and for $\theta \geq 80°$ there a very slight noise excess. This noise excess is probably due to the increase in TKE on the top of the jet. In case 4Va, the TKE reductions are larger and occur over a longer axial extent of about $4D_f$. The sideline TKE is reduced appreciably but less than the downward TKE. Correspondingly, the peak OASPL is reduced by 4.8 dB in the downward direction and 4.0 dB in the sideline direction. There is a significant increase of the TKE on the top of the jet, which may be responsible for a small (but important for perceived noise) uplift of the OASPL curves at large angles. Past works have recognized the adverse impact excess noise

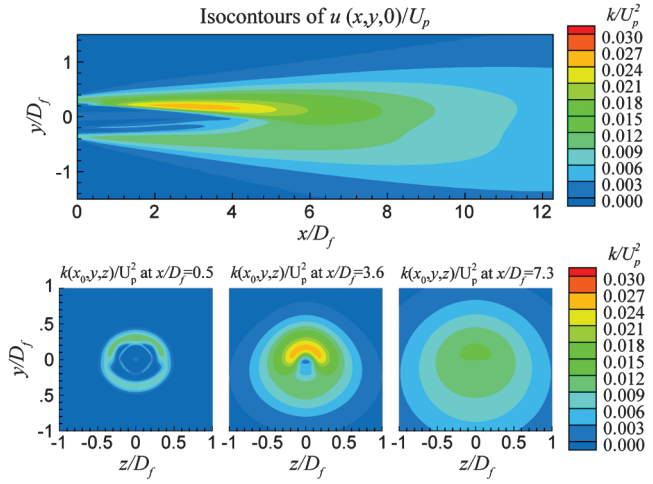

Fig. 20 Turbulent kinetic energy field for configuration 4Vc at hot set point.

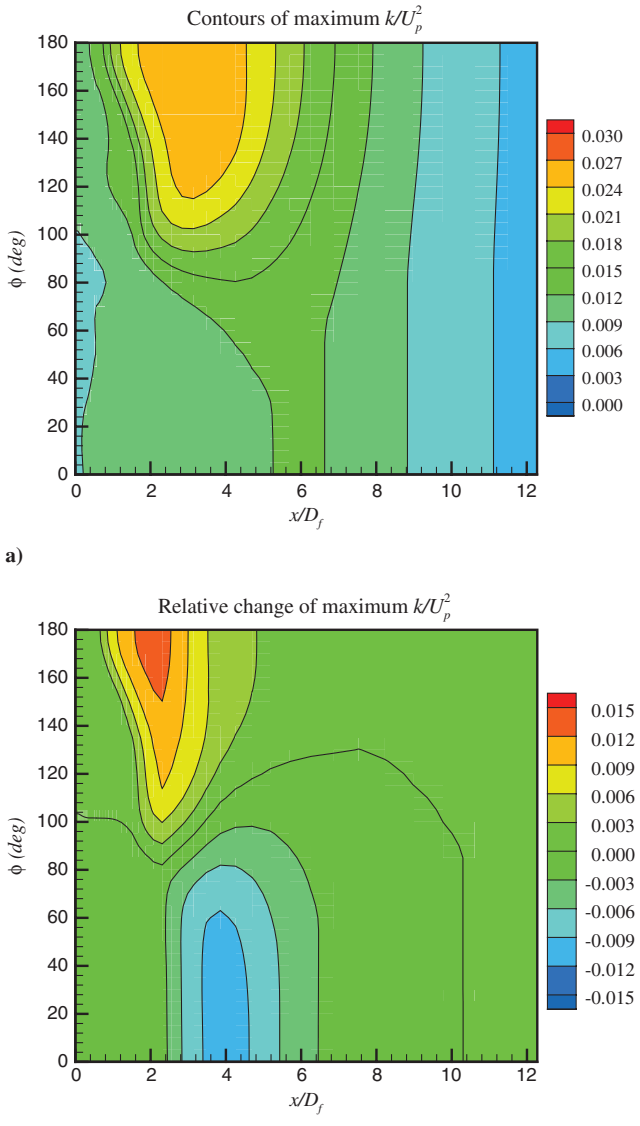

Fig. 21 Azimuthal variation of $k_{\max}$ for case 4Vc at hot set point. a) absolute levels and b) levels relative to baseline.

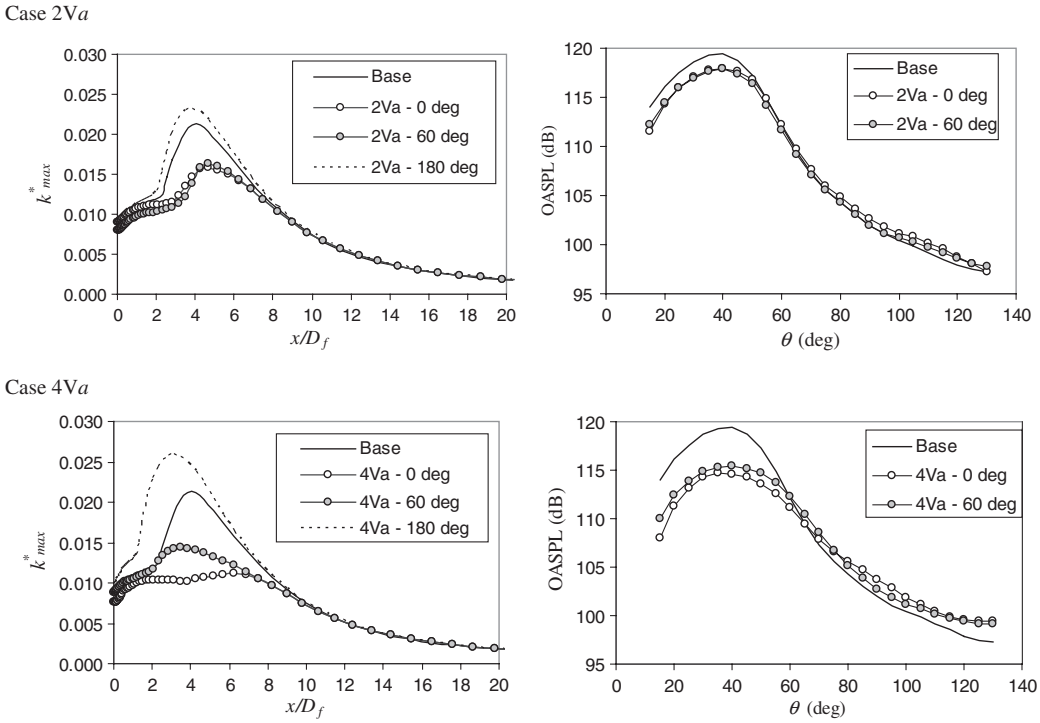

Fig. 22 Axial distribution of maximum turbulent kinetic energy and OASPL directivity for cases 2Va and 4Va.

on the top of the jet can have on downward noise emission at large polar angles [14,15].

We now attempt a quantitative correlation between the experimental reduction in peak OASPL, listed in Table 2, with the reduction of TKE predicted by the computations and exemplified in Fig. 22. The far-field pressure spectrum $S(\omega)$ in a particular polar/azimuthal direction is produced by the volume integral of an equivalent noise source q radiating in that direction:

$$S(\omega, \theta, \phi) = \frac{1}{R^2} \int_V q(\mathbf{x}, \omega, \theta, \phi)\, \mathrm{d}\mathbf{x} \tag{8}$$

where R is the distance of the observer from the jet. The term q in Eq. (8) represents the cross-spectral density of the Lighthill stress tensor with appropriate inclusion of time delays, source convection effects, spatial correlation length scales, and dimensional constant [3–5]. Integrating over frequency we relate the variance of the pressure to the variance of the equivalent noise source:

$$\sigma_p^2(\theta, \phi) = \frac{1}{R^2} \int_V \sigma_q^2(\mathbf{x}, \theta, \phi)\, \mathrm{d}\mathbf{x} \tag{9}$$

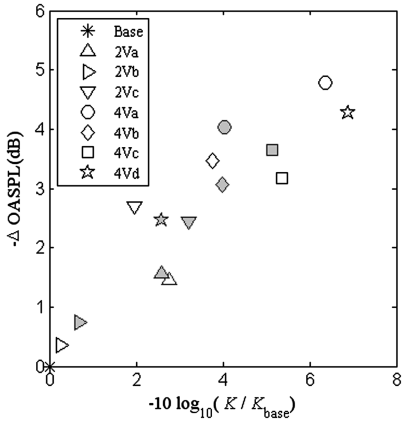

Fig. 23 Reduction in peak OASPL versus reduction in TKE-based noise source strength K. Open symbols: downward; grayed symbols: sideline.

We now consider the polar direction of peak emission and approximate the jet as a line source with the source strength scaling $k^n_{\max}(x, \phi)$. The volume integral is reduced to a line integral along the jet centroid, which, for practical purposes, is equivalent to integration along the nozzle axis x:

$$\sigma^2_{p_{\max}}(\phi) = \frac{C}{R^2} \int_0^L k^n_{\max}(x, \phi)\, \mathrm{d}x = \frac{C}{R^2} K(\phi) \tag{10}$$

where the integral has been symbolized $K(\phi)$ and C is a dimensional constant. This type of one-dimensional representation of the jet source strength can be found in reduced acoustic analogy models [34] and in acoustic imaging methods (e.g., [35,36]). Recognizing that the OASPL is the variance of the pressure in decibel scale,

$$\mathrm{OASPL}_{\max}(\phi) = 10 \log_{10}[K(\phi)] + \mathrm{const} \tag{11}$$

Further, the OASPL change relative to the axisymmetric baseline is

$$\Delta\mathrm{OASPL}_{\max}(\phi) = 10 \log_{10}\left[\frac{K(\phi)}{K_{\mathrm{base}}}\right] \tag{12}$$

To evaluate K we used $n = 7/2$, consistent with the prevailing acoustic analogy models [3–5]. The integration of Eq. (10) started from the plug tip to the end of the domain at $x = 22D_f$. Figure 23 plots the left- and right-hand sides of Eq. (12) for the five cases in which we have acoustic measurements of OASPL and computations of the TKE. The correlation comprises downward ($\phi = 0°$) and sideline ($\phi = 60°$) evaluations of the two terms. An approximately linear trend is obtained, suggesting that Eq. (12) indeed holds, although in a proportional, not exact, sense. Had we used $n = 3$, a least-squares fit of the data would satisfy exactly Eq. (12), but identifying the proper power law for k was beyond the scope of this work. The significant conclusion is that there is a strong correlation between the TKE reduction and the suppression of peak OASPL. We emphasize that this correlation should be viewed in the context of this study, that is, redistribution of TKE from a known baseline condition, with applicability to noise in the peak radiation direction. Even though the scope of the correlation is limited, it is valuable for our efforts in designing quieter fan flow deflection configurations. The validated RANS code is maturing such that it can generate reasonable predictions of OASPL reduction based on the computed

redistribution of the TKE field. We consider this an important first step toward RANS becoming a design tool for these nozzle configurations.

VIII. Conclusions

A computational and experimental study was conducted for a dual-stream supersonic turbofan engine with several fan flow deflector configurations. The aim of the investigation was to validate a RANS computational model of the jet flow with experimental results, determine the effects of hot and cold operating conditions on the jet velocity profile and turbulent kinetic energy, study the turbulent kinetic energy effects of different fan flow deflection configurations, and investigate the connection between noise reduction and the turbulent kinetic energy in the jet plume in various propagation directions.

The computational validation was performed by comparing mean velocity fields, radial velocity gradient fields and inflectional layer plots experimental results. The computational results agreed well with the experimental results for all cases. The comparison of hot and cold jets indicated, as expected, that the hot jet has higher levels of mixing giving a larger growth rate and shorter potential core. When the axial distance was nondimensionalized by the potential core lengths of the hot and cold jets, respectively, the velocity profiles almost collapsed on the same curve, indicating the physical elements of the jet are reasonably consistent regardless of the temperature.

For the fan flow deflection configurations, computations show a decrease in turbulent kinetic energy k on the underside of the jet and an increase in k on top of the jet. An overall noise source term is modeled as the axial integral of $k_{\max}^{7/2}$, where $k_{\max}$ is the axial distribution of maximum k for a given azimuth angle. A strong correlation is found between the reduction in the level of the modeled noise source term and the reduction in the peak level of the overall sound pressure level. This constitutes an initial step toward predictive methods that will enable the design of efficient fan flow deflection schemes for supersonic and subsonic applications.

Acknowledgments

The support by NASA Cooperative Agreement NNX07AC62A (monitored by K. B. M. Q. Zaman) is gratefully acknowledged. We thank Vincent Phong for his assistance with the design and fabrication of the vanes.

References

[1] Ko, N. W. M., and Kwan, A. S. H., "The Initial Region of Subsonic Coaxial Jets," *Journal of Fluid Mechanics*, Vol. 73, Part 2, 1976, pp. 305–332. doi:10.1017/S0022112076001389

[2] Fisher, M. J., Preston, G. A., and Bryce, W. D., "A Modelling of the Noise from Simple Coaxial Jets, Part 1: With Unheated Primary Flow," *Journal of Sound and Vibration*, Vol. 209, No. 3, 1998, pp. 385–403. doi:10.1006/jsvi.1997.1218

[3] Morris, P. J., and Farassat, F., "Acoustic Analogy and Alternative Theories for Jet Noise Prediction," *AIAA Journal*, Vol. 40, No. 4, 2002, pp. 671–680. doi:10.2514/2.1699

[4] Self, R. H., and Azarpeyvand, M., "Jet Noise Prediction Using Different Turbulent Scales," *Acoustical Physics*, Vol. 55, No. 3, 2009, pp. 433–440. doi:10.1134/S106377100903021X

[5] Birch, S. F., Lyubimov, D. A., Maslov, V. P., Secundov, A. N., and Yakubosky, Y., "A RANS based Jet Noise Prediction Procedure," AIAA Paper 2007-3727, May 2007.

[6] Troutt, T. R., and McLaughlin, D. K., "Experiments on the Flow and Acoustic Properties of a Moderate-Reynolds-Number Supersonic Jet," *Journal of Fluid Mechanics*, Vol. 116, 1982, pp. 123–156. doi:10.1017/S0022112082000408

[7] Tam, C. K. W., and Burton, D. E., "Sound Generation by the Instability Waves of Supersonic Flows. Part 2. Axisymmetric Jets," *Journal of Fluid Mechanics*, Vol. 138, 1984, pp. 273–295. doi:10.1017/S0022112084000124

[8] Panda, J., Seasholtz, R. G., and Elam, K. A., "Investigation of Noise Sources in High-Speed Jets via Correlation Measurements," *Journal of Fluid Mechanics*, Vol. 537, 2005, pp. 349–385. doi:10.1017/S0022112005005148

[9] Papamoschou, D., "New Method for Jet Noise Suppression in Turbofan Engines," *AIAA Journal*, Vol. 42, No. 11, 2004, pp. 2245–2253. doi:10.2514/1.4788

[10] Papamoschou, D., and Debiasi, M., "Conceptual Development of Quiet Turbofan Engines for Supersonic Aircraft," *Journal of Propulsion and Power*, Vol. 19, No. 2, 2003, pp. 161–169. doi:10.2514/2.6103

[11] Papamoschou, D., and Nielsen, P., "Fan Flow Deflection for Supersonic Turbofan Engines," AIAA Paper 2008-0039, Jan. 2008.

[12] Zaman, K., "Noise- and Flow-Field of Jets from an Eccentric Coannular Nozzle," AIAA Paper 2004-0005, Jan. 2004.

[13] Papamoschou, D., "Fan Flow Deflection in Simulated Turbofan Exhaust," *AIAA Journal*, Vol. 44, No. 12, 2006, pp. 3088–3097. doi:10.2514/1.22552

[14] Papamoschou, D., "Pylon-Based Jet Noise Suppressors," *AIAA Journal*, Vol. 47, No. 6, 2009, pp. 1408–1420. doi:10.2514/1.37780

[15] Dippold, V., Foster, L., and Wiese, M., "Computational Analyses of Offset Stream Nozzles for Noise Reduction," *Journal of Propulsion and Power*, Vol. 25, No. 1, 2009, pp. 204–217. doi:10.2514/1.34943

[16] Viswanathan, K., Shur, M., Spalart, P. R., and Strelets, M., "Flow and Noise Predictions for Single and Dual-Stream Beveled Nozzles," *AIAA Journal*, Vol. 46, No. 3, 2008, pp. 601–626. doi:10.2514/1.27299

[17] DeBonis, J. R., "RANS Analyses of Turbofan Nozzles With Internal Wedge Deflectors for Noise Reduction," *Journal of Fluids Engineering*, Vol. 131, Apr. 2009, Paper 041104. doi:10.1115/1.3089536

[18] Saiyed, N. H., Mikkelsen, K. L., and Bridges, J. E., "Acoustics and Thrust of Separate-Flow High-Bypass-Ratio Engines," *AIAA Journal*, Vol. 41, No. 3, 2003, pp. 372–378. doi:10.2514/2.1986

[19] Papamoschou, D., "Acoustic Simulation of Coaxial Hot Air Jets Using Cold Helium-Air Mixture Jets," *Journal of Propulsion and Power*, Vol. 23, No. 2, 2007, pp. 375–381. doi:10.2514/1.21776

[20] Savitzky, A., and Golay, M. J. E., "Smoothing and Differentiation of Data by Simplified Least Squares Procedures," *Analytical Chemistry*, Vol. 36, No. 8, 1964, pp. 1627–1639. doi:10.1021/ac60214a047

[21] Smyth, W. D., and Moum, J. N., "Shear Instability and Gravity Wave Saturation in an Asymmetrically Stratified Jet," *Dynamics of Atmospheres and Oceans*, Vol. 35, 2002, pp. 265–294. doi:10.1016/S0377-0265(02)00013-1

[22] Simmons, J. M., Platzer, M. F., and Smith, T. C., "Velocity Measurement in an Oscillating Plane Jet Issuing into a Moving Air Stream," *Journal of Fluid Mechanics*, Vol. 84, Part 1, 1978, pp. 33–53. doi:10.1017/S0022112078000038

[23] Jameson, A., Schmift, W., and Turkel, E., "Numerical Solutions of the Euler Equations by Finite Volume Methods Using Runge–Kutta Time Stepping Scheme," AIAA Paper 1981-1259, Jan. 1981.

[24] Baldwin, B. S., and Lomax, H., "Thin-Layer Approximation and Algebraic Model for Separation Flows," AIAA Paper 1978-257, 1978.

[25] Spalart, P. R., and Allmaras, S. R., "A One-Equation Turbulence Model for Aerodynamic Flows," AIAA Paper 1992-0439, Jan. 1992.

[26] Wilcox, D. C., "Reassessment of the Scale Determining Equation for Advanced Turbulence Models," *AIAA Journal*, Vol. 26, No. 11, 1988, pp. 1299–1310. doi:10.2514/3.10041

[27] Menter, F. R., "Two-Equation Eddy-Viscosity Turbulence Models for Engineering Applications," *AIAA Journal*, Vol. 32, No. 8, 1994, pp. 1598–1605. doi:10.2514/3.12149

[28] Turkel, E., "A Review of Preconditioning Methods for Fluid Dynamics," *Applied Numerical Mathematics*, Vol. 12, No. 1, 1993, pp. 257–284. doi:10.1016/0168-9274(93)90122-8

[29] Liu, F., and Zheng, X., "A Strongly Coupled Time-Marching Method for Solving the Navier–Stokes and k-ω Turbulence Model Equations with Multigrid," *Journal of Computational Physics*, Vol. 128, No. 2, 1996, pp. 289–300. doi:10.1006/jcph.1996.0211

[30] Sadeghi, M., "Parallel Computation of Three-Dimensional Aeroelastic Fluid-Structure Interaction," Ph.D. Dissertation, Univ. of California,

Irvine, Irvine, CA, 2004.
[31] Bohbot, J., Grondin, D., and Darracq, D., "A Parallel/Multigrid Conservative Patched/Sliding Mesh Algorithm for Turbulent Flow Computations of 3D Complex Aircraft Configurations," AIAA Paper 2001-1006, Jan. 2001.
[32] Bridges, J., "Effect of Heat on Space-Time Correlations in Jets," AIAA Paper 2006-2534, May 2006.
[33] Bridges, J., and Wernet, M., "Effect of Temperature on Jet Velocity Spectra," AIAA Paper 2007-3628, May 2007.
[34] Self, R. H., "Jet Noise Prediction Using the Lighthill Acoustic Analogy," *Journal of Sound and Vibration*, Vol. 275, 2004, pp. 757–768. doi:10.1016/j.jsv.2003.06.020
[35] Fisher, M. J., Harper-Bourne, M., and Glegg, S. A. L., "Jet Engine Source Location: The Polar Correlation Technique," *Journal of Sound and Vibration*, Vol. 51, No. 1, 1977, pp. 23–54. doi:10.1016/S0022-460X(77)80111-9
[36] Billingsley, J., and Kinns, R., "The Acoustic Telescope," *Journal of Sound and Vibration*, Vol. 48, No. 4, 1976, pp. 485–510. doi:10.1016/0022-460X(76)90552-6

A. Lyrintzis
Associate Editor